Supplementary Information (SI) for Journal of Materials Chemistry A.

Supporting Information

Supramolecular Donor-Acceptor Engineering Enables Efficient Intermolecular Charge Separation for Enhanced Photocatalytic Hydrogen Production

Jicheng Xu[ab‡], *Jingfan Shao* [ab‡], *Lujie Jin*[ac], *Yuchen Yan*[ab], *Youyong Li* [ac], *Yujin Ji**[ac], *Yanguang Li**[ab], *Wei Huang**[ab]

[a] Institute of Functional Nano & Soft Materials (FUNSOM), Soochow University, Suzhou, 215123 China.

[b] Jiangsu Key Laboratory for Advanced Negative Carbon Technologies, Soochow University, Suzhou 215123, China

[c] State Key Laboratory of Bioinspired Interfacial Materials Science, Suzhou 215123, China

[‡] These authors contributed equally.

Correspondence to: yanguang@suda.edu.cn; weihuang@suda.edu.cn; yjji@suda.edu.cn

Experimental methods

Chemicals

All chemicals were purchased and used without further purification. Imidazole, 3,4,9,10-perylenetetracarboxylic dianhydride (PTCDA), aminomethylphosphonic acid (AMPA), sodium hydroxide (NaOH), 1-pyrenebutyric acid (PBA), ascorbic acid (AA), chloroplatinic acid (H_2PtCl_6) and ethanol were purchased from Aladdin Reagent Co., Ltd., Shanghai, China. Hydrochloric acid (HCl) aqueous solution (36 wt%) was purchased from Yonghua Chemical Co., Ltd., Jiangsu, China. All the solvents and chemicals were used as received without further purification. Deionized water was prepared using a Milli-Q purification system.

Material synthesis

Synthesis of N,N′-bis(phosphonomethyl)perylene-3,4,9,10-tetracarboxylic diimide (PPDI)

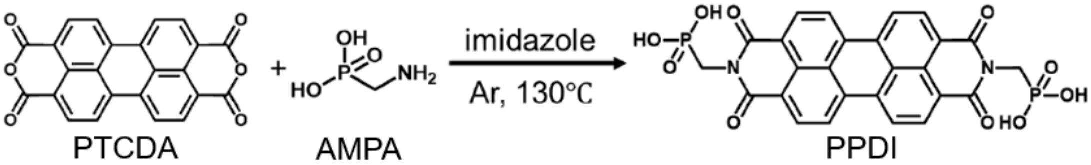

PPDI was synthesized according to previous literature (*ACS Appl. Mater. Interfaces* **2014**, 6, 16). In a typical procedure, 15 g of imidazole (0.22 mol), 790 mg of PTCDA (2.0 mmol), and 470 mg of AMPA (4.2 mmol) were charged into a 100 mL three-neck flask. After degassing by bubbling argon for 15 minutes, the flash was heated to 130°C, and maintained at this temperature for 40 minutes under argon atmosphere. After cooled down to room temperature, a mixed solution of 25 mL of HCl and 25 mL of ethanol was added to the reaction mixture before the mixture was vigorously stirred for 30 minutes. The precipitate was then collected by centrifugation, thoroughly washed with 2 M HCl and ethanol, and subsequently dried under vacuum at 80°C. The product was achieved as a deep red powder with a yield of 90%. ^1H NMR (400 MHz, D_2O) δ (ppm) = 8.45 – 7.20 (broad, 8H), 4.51 – 4.14 (broad, 4H); ^{31}P NMR (400 MHz, D_2O) δ (ppm) = 14.09. The spectral features are consistent with those reported in the literature (Fig. S1 and Fig. S2)

Preparation of PPDI@PBA-x

PPDI@PBA-x was prepared by acid-induced precipitation method. Taking PPDI@PBA-1 for example, 100 mg of PPDI (0.17 mmol) and 49 mg of PBA (0.17 mmol) were dissolved in 24 mL of 0.1 M NaOH. Subsequently, 5 mL of 2 M HCl was poured into the above solution to precipitate out the D-A assemblies. The precipitate was collected by centrifugation and washed several times with 0.1 M HCl, followed by dried under vacuum at 80°C to obtain the PPDI@PBA-1 as a dark-red powder.

Other D-A samples were prepared under identical conditions, except that 5, 17, 100, 150, 250 and 500 mg of PBA was used for PPDI@PBA-10, 3, 0.5, 0.3, 0.2 and 0.1 respectively. Pristine PPDI and PBA were also prepared following the same procedure, except that PBA or PPDI was omitted, respectively.

Characterizations

Liquid ^1H and ^{31}P nuclear magnetic resonance (NMR) were performed on a 400 MHz Bruker Avance NMR spectrometer. Fourier-transform infrared (FT-IR) spectra were collected on a Bruker Vertex 70 FTIR spectrometer under the attenuated total reflection (ATR) mode. Scanning electron microscopy (SEM) images were taken on a ZEISS Gemini 500 scanning electron microscope. Transmission electron microscopy (TEM) images and energy-dispersive X-ray spectroscopy (EDS) mapping were carried out on a Thermo Scientific Talos F200X scanning/transmission electron microscope at 200 kV. Powder X-ray diffraction (PXRD) was conducted on a PANalytical X-ray diffractometer with monochromatic Cu Kα radiation. Raman spectroscopy was performed on the Horiba Jobin-Yvon LabRam HR800 Raman spectrometer with a laser of 532 nm wavelength. Ultraviolet-visible (UV-vis) diffuse reflectance spectra of the solid samples were recorded on a Perkin Elmer Lambda 950 spectrophotometer using $BaSO_4$ as a reference. Steady-state photoluminescence (PL) and time-resolve PL spectra were measured on a Hamamatsu Quantaurus-Tau fluorescence lifetime spectrometer. X-ray Photoelectron spectroscopy (XPS) results were obtained on a Thermo Scientific K-Alpha X-ray photoelectron spectrometer. Electron paramagnetic resonance (EPR) analyses were conducted on a Bruker A300 spectrometer under visible light irradiation (λ>420 nm) at room temperature. Ultraviolet photoelectron spectroscopy (UPS) was performed on an Ultra DLD X-ray photoelectron spectrometer with a helium discharge lamp using the He I (21.22 eV) radiation line.

Femtosecond transient absorption spectroscopy (fs-TAS)

Femtosecond transient absorption spectroscopy (fs-TAS) were conducted using a TA100 spectrometer (Time-Tech Spectra). The system was driven by a fiber laser equipped with an optical parametric amplifier (OPA), delivering 260 fs pulses at 1030 nm with a pulse energy of 100 μJ and a repetition rate of 100 kHz. The probe light was a supercontinuum white-light continuum (480–900 nm) generated by focusing the 1030 nm laser into a 6 mm sapphire crystal. The pump pulses (445 nm) were obtained via OPA frequency conversion. Pump and probe beams were spatially and temporally overlapped on the sample using an optical delay line. The pump beam was modulated at 500 Hz with a mechanical chopper and attenuated by neutral density filters. The transmitted probe light was collected by a fiber-coupled monochromator and detected using a CMOS array detector.

EPR measurements

10 mg of the solid sample was packed into an EPR tube with an inner diameter of 1 mm to form a columnar sample approximately 2 cm in length. EPR signals were collected either in dark or when irradiated by a 300W-Xenon lamp ($\lambda > 420$ nm).

Photocurrent measurements

Photocurrent response was carried out on a standard three-electrode system, controlled by a CHI 660E potentiostat. A Pt gauze, a saturated calomel electrode (SCE), a piece of photocatalyst-coated fluorine-doped tin oxide (FTO) glass were used as the counter electrode, reference electrode and working electrode, respectively. 0.2 M Na_2SO_4 aqueous solution was used as the electrolyte. To prepare the working electrode, 2 mg of catalyst powder was ultrasonically dispersed in 2 mL of 0.1 M HCl solution before dropcasted onto a piece of FTO glass with an exposed area of 1×1 cm^2. The photocurrent measurements were conducted at a bias voltage of +0.1 V vs. SCE by directly irradiating the working electrode from the back side, using a 300 W xenon lamp equipped with a 420 nm cut-off filter.

Photocatalytic hydrogen production

In a typical experiment, 5 mg catalyst was ultrasonically dispersed in 50 mL of 0.1 M AA aqueous solution in a 400 mL top-irradiated photocatalyst reactor. Following that, a calculated amount of H_2PtCl_6 aqueous solution (corresponding to ~3 wt% Pt relative to the photocatalyst) was introduced into the reaction solution. The mixture was carefully evacuated three times to remove air and refilled with argon. For the photocatalytic tests, the reaction mixture was top-irradiated with a 300 W Xe lamp (Beijing China Education Au-light, CEL-HXF300) equipped with a 420 nm cut-off filter. The light intensity was controlled at 300 mW cm^{-2}, and the reaction temperature was maintained at 25℃ by a water-cooled system. The amount of H_2 was quantified using an off-line gas chromatograph (SHIMADZU 2010, GC-2014) equipped with a TCD detector using Ar as the carrier gas, based on an external calibration curve (Fig. S19).

Apparent quantum efficiency (AQE) measurements

Typically, 5 mg of PPDI@PBA-1 deposited 3 wt% Pt cocatalyst were dispersed in 50 mL of 0.1 M AA aqueous solution. The solution was degassed and irradiated by a 300 W Xe-lamp with monochromatic light (λ = 420, 450, 500, 550 or 650 nm). The light intensity was adjusted to be 5.5 mW cm^{-2} using an optical power detector (Newport, Model 1918-R). The illumination area was controlled to be 1 cm^2. The AQE value was calculated using the following equation:

$$\text{AQE (\%)} = \frac{2nN_\text{A}hc}{ISt\lambda} \times 100\%$$

where n is the molar amount of hydrogen produced (mol), N_A is the Avogadro constant (6.022×10^{23} mol^{-1}), h is the Planck constant (6.626×10^{-34} J·s), c is the speed of light (3×10^8 m s^{-1}), S is the irradiation area (cm^2), I is the light intensity (W cm^{-2}), t is the irradiation time (s) and λ is the wavelength of the incident light (m).

Computational Details

All Density Functional Theory (DFT) calculations were performed using the Gaussian 16 software package (Gaussian 16, Revision A.01. Wallingford, CT: Gaussian Inc (2016)). The molecular geometries of PBA, PDI, and their stacked complexes were fully optimized in the gas phase. The B3LYP hybrid functional (*J. Phys. Chem.* **1994**, *98*, 45) was employed in conjunction with the 6-

311G(d) basis set for all atoms. To accurately describe the non-covalent interactions, particularly the π-π stacking effects prevalent in these aromatic systems, Grimme's D3 dispersion correction with Becke-Johnson damping (*J. Comput. Chem.* **2011**, *32*, 7) was included in the calculations.

The electronic structures were analyzed based on the optimized geometries. The highest occupied molecular orbital (HOMO) and the lowest unoccupied molecular orbital (LUMO), as well as the molecular dipole moments, were calculated to evaluate the electronic properties. Molecular electrostatic potential (ESP) maps were generated to visualize the charge distribution, since the red and blue regions correspond to negative and positive electrostatic potentials, respectively. The binding energy (E_b) of the stacked complexes was calculated using the equation: $E_\mathrm{b} = E_\mathrm{complex} - (E_\mathrm{monomer1} + E_\mathrm{monomer2})$, where E_complex is the total energy of the stacked dimer, and E_monomer represents the total energy of the isolated monomers. All molecular structures, orbitals, and electrostatic potential surfaces were visualized using GaussView.

Supplementary figures

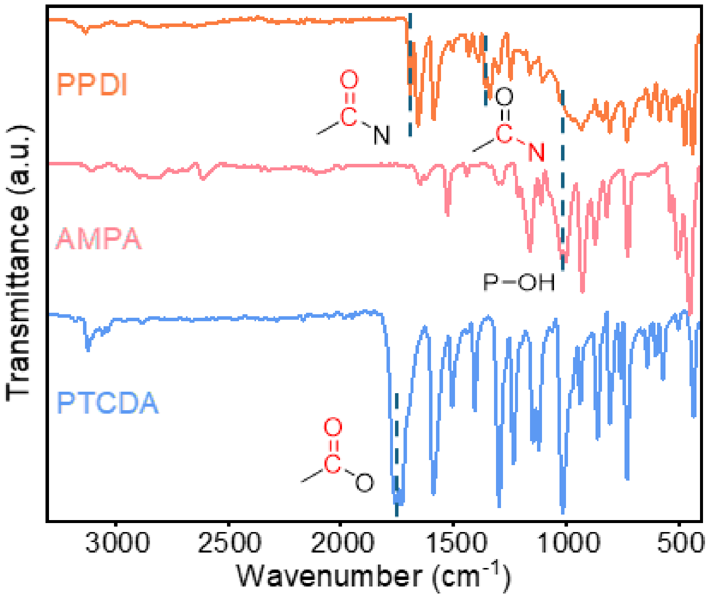

Fig. S1 FT-IR spectra of PTCDA, AMPA and PPDI.

Note: Compared to the spectra of the precursors, the FT-IR spectrum of PPDI exhibits new absorption bands at 1692 and 1358 cm^{-1}, corresponding to the characteristic stretching vibrations of C=O and C-N bonds in imide units, respectively (*Chem. Commun.* **2019**, *55*, 8090). The band at 1026 cm^{-1} could be assigned to the terminal phosphate group (*J. Mater. Chem. A* **2021**, *9*, 7675).

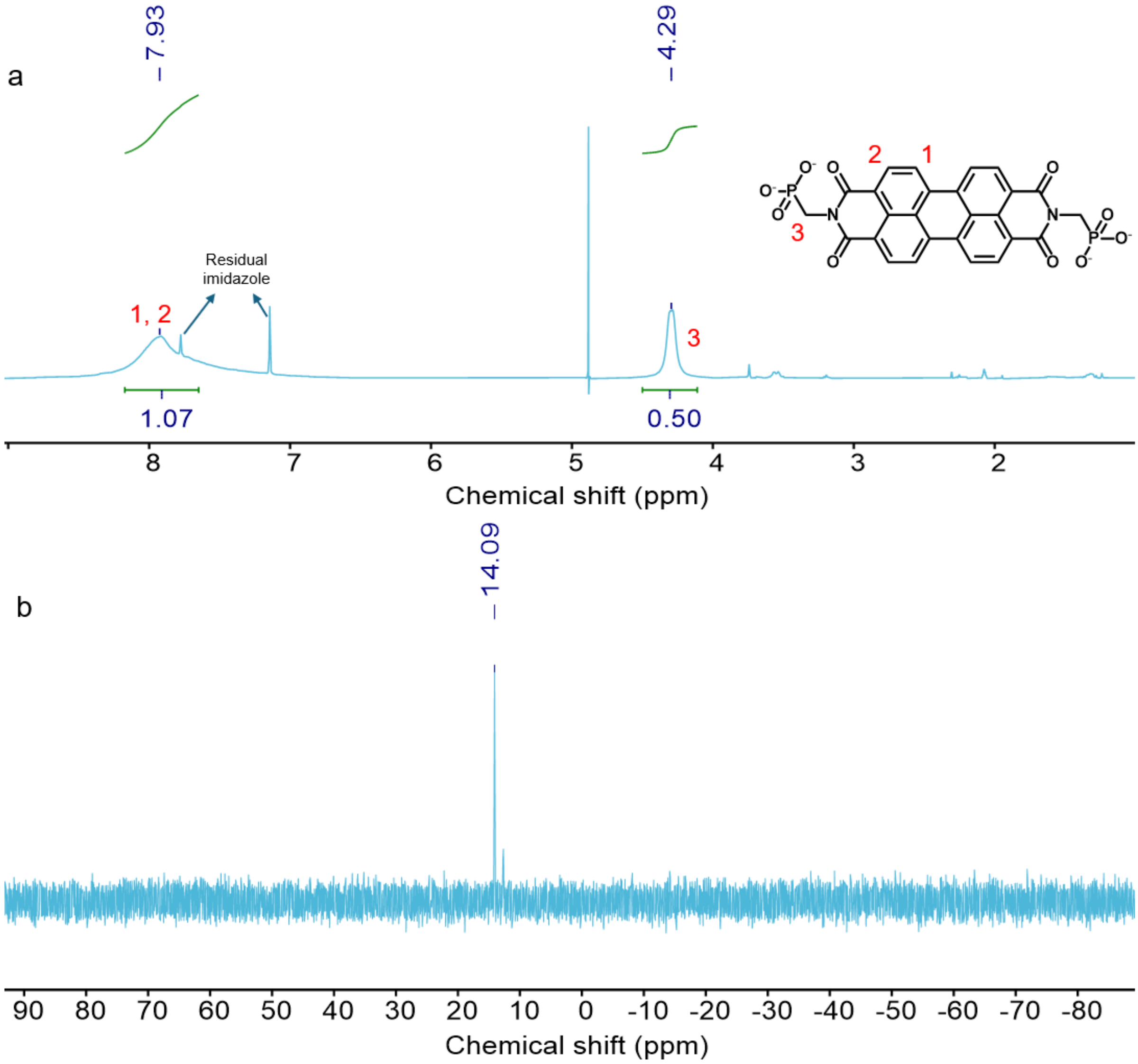

Fig. S2 ^{1}H and ^{13}P NMR of PPDI.

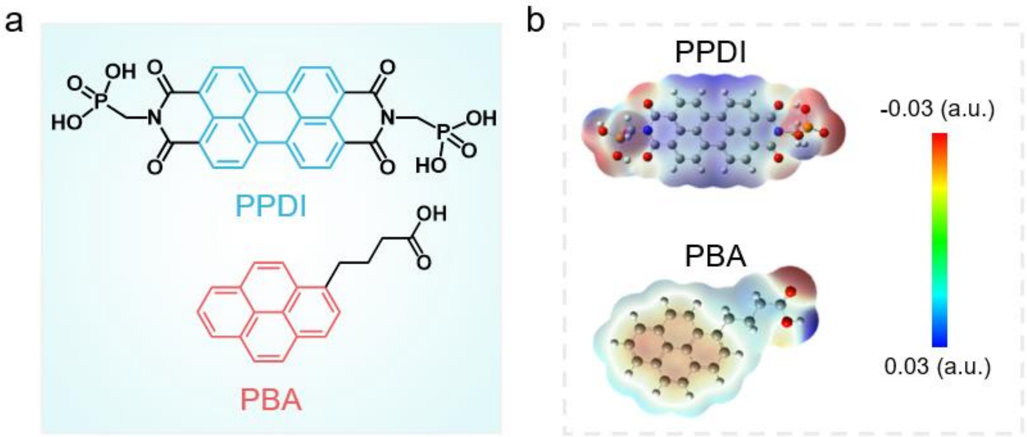

Fig. S3 (a) Molecular formula of PPDI and PBA. (b) ESP mapping that showing the charge distribution of PPDI and PBA.

Note: The ESP results show that PPDI has an electron-deficient nature while PBA is electron-rich. The opposite ESP distributions of PPDI and PBA on the aromatic cores favor their spontaneous association through favorable electronic interactions.

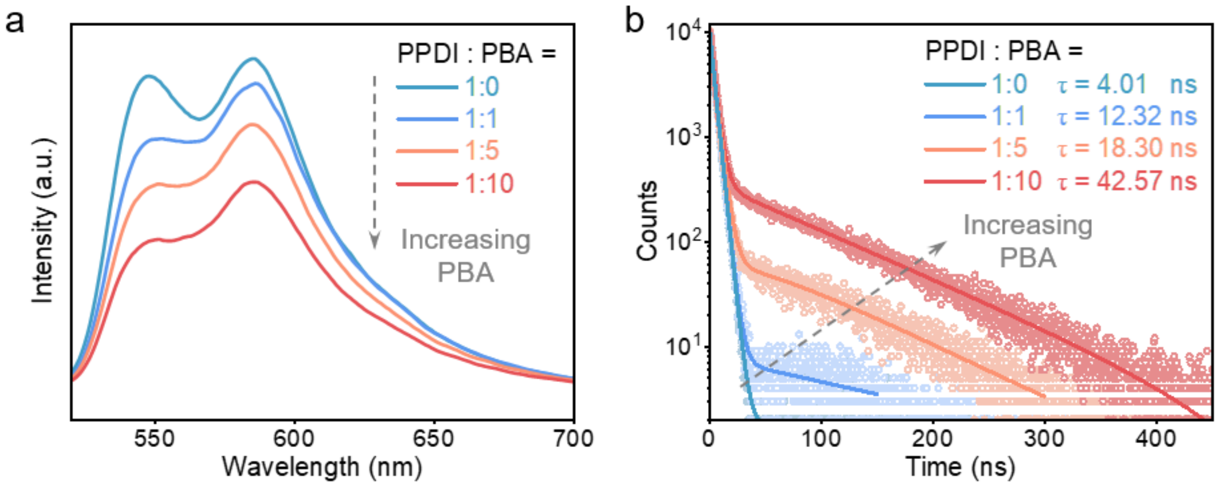

Fig. S4 (a) Steady-state PL spectra and (b) time-resolved PL spectra of the mixed solution of PPDI and PBA with different molar ratios.

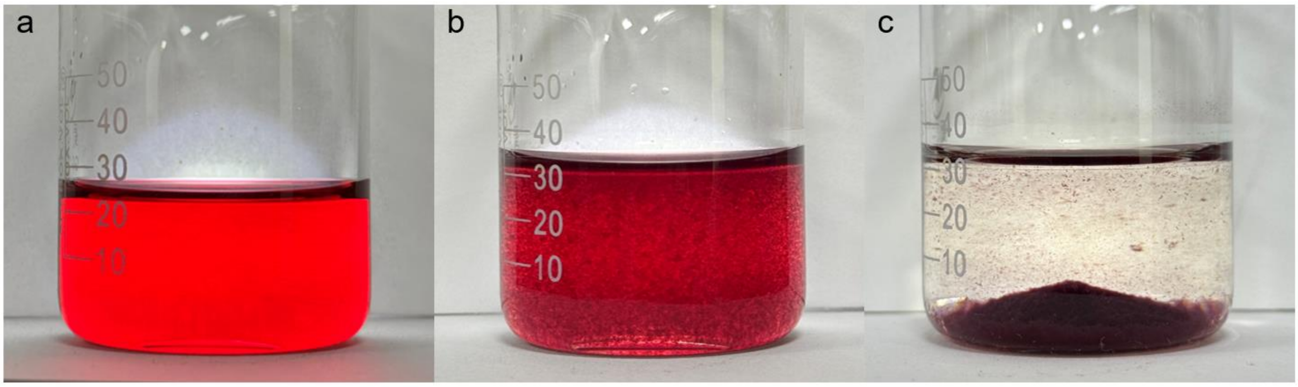

Fig. S5 (a) Solution of equimolar PPDI and PBA in 0.1 M NaOH solution. (b) Excess 2M HCl solution was added, leading to the rapid precipitation of PPDI@PBA-1. (c) PPDI@PBA-1 was settled on the bottom of the beaker without stirring.

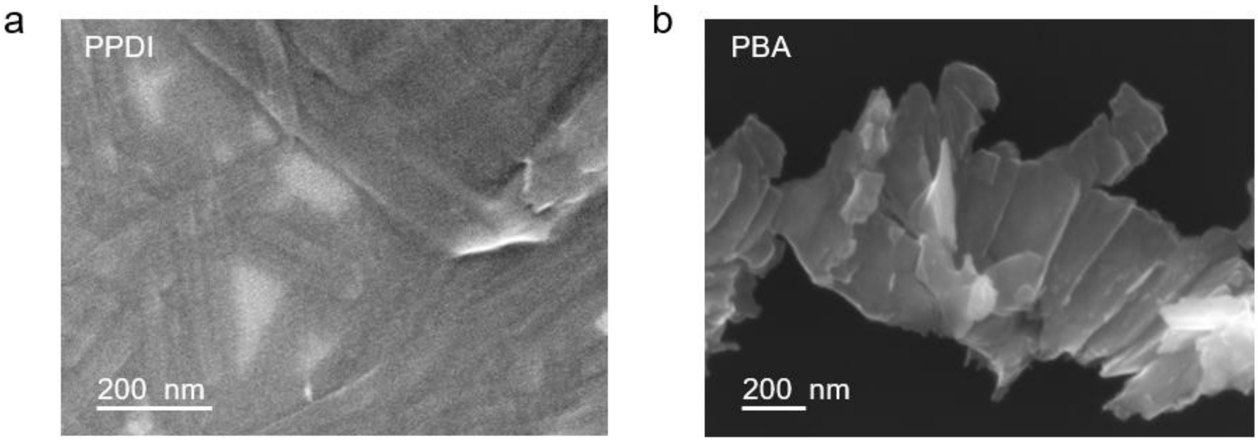

Fig. S6 SEM images of pristine (a) PPDI and (b) PBA.

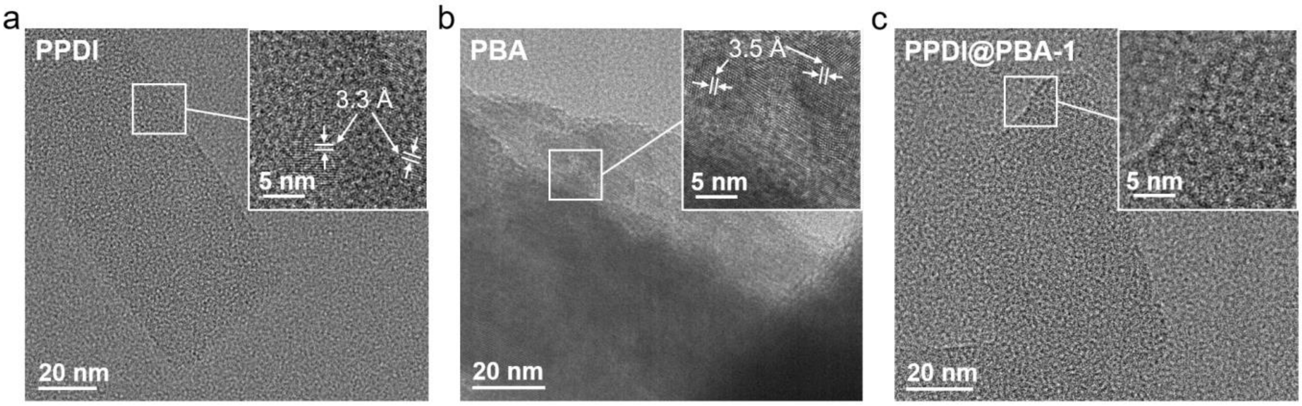

Fig. S7 High resolution-TEM images of (a) PPDI and (b) PBA and (c) PPDI@PBA-1.

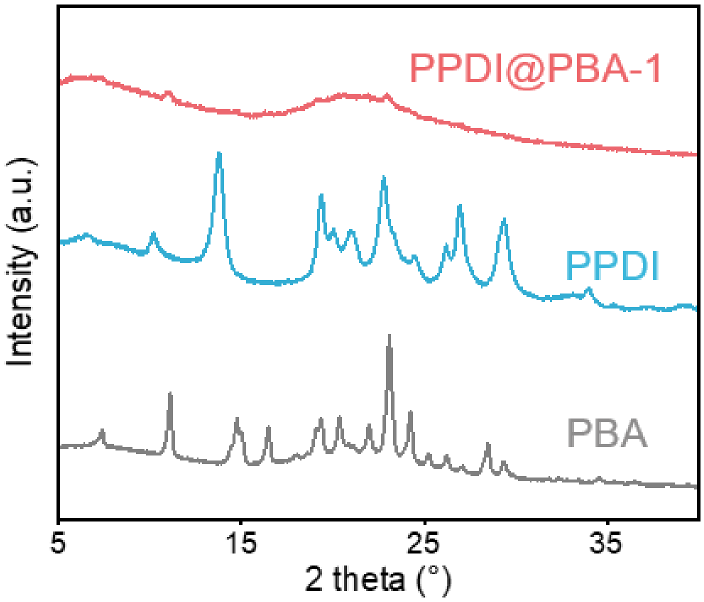

Fig. S8 PXRD patterns of PPDI, PBA and PPDI@PBA-1.

Fig. S9 Photographs of PPDI@PBA-x samples and their water contact-angles.

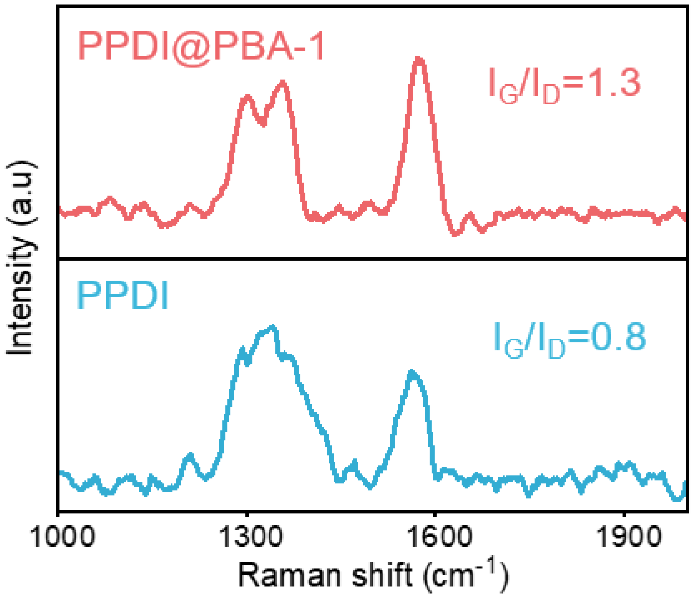

Fig. S10 Raman spectra of PPDI and PPDI@PBA-1.

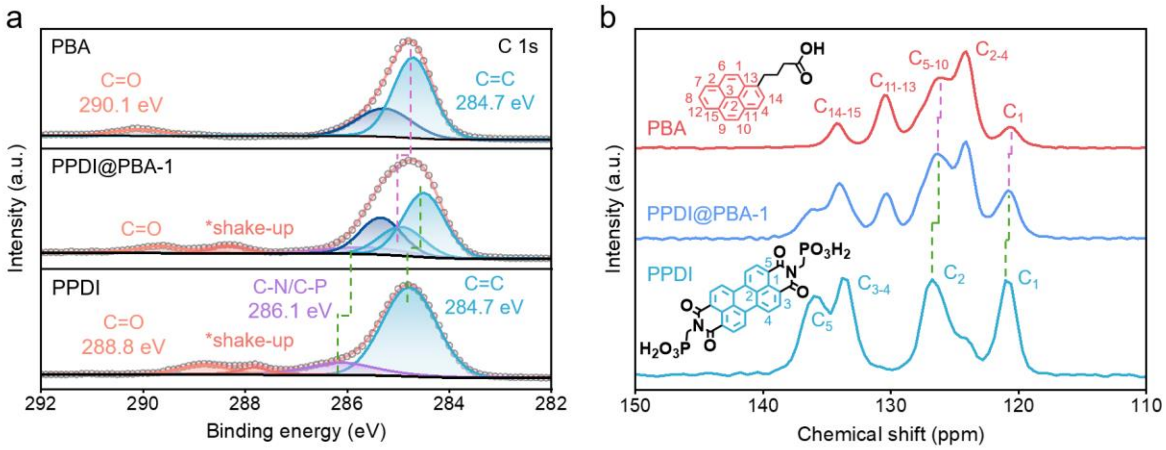

Fig. S11 (a) C 1s XPS and (b) solid-state ^{13}C NMR spectra of PBA, PPDI@PBA-1 and PPDI.

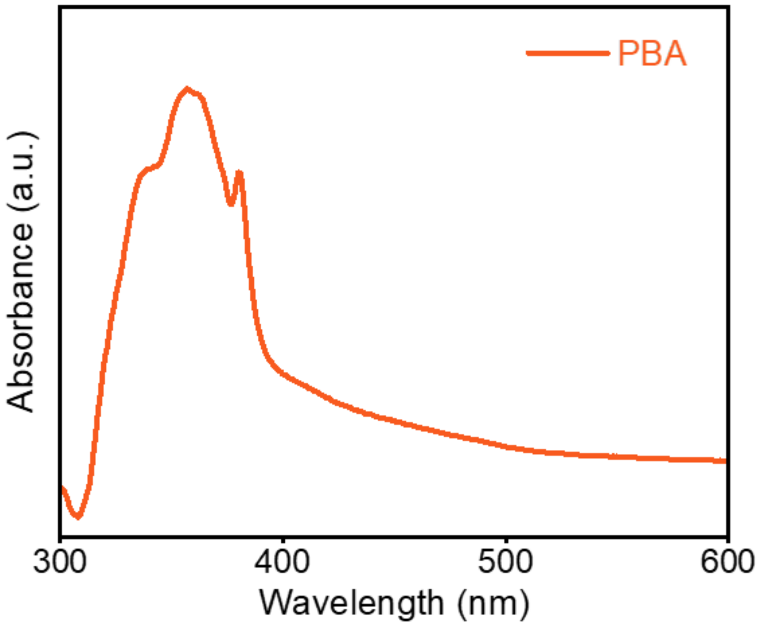

Fig. S12 UV-vis diffuse reflection spectrum of pristine PBA.

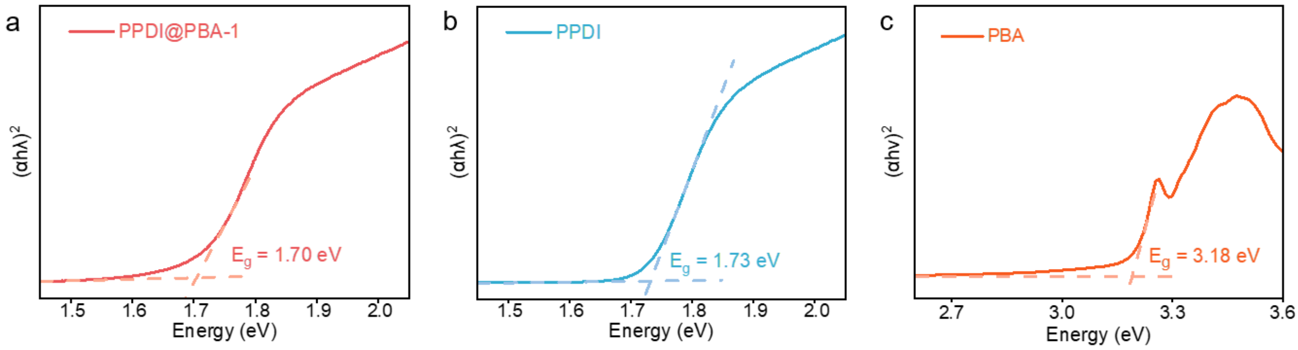

Fig. S13 Tauc plots of (a) PPDI, (b) PPDI@PBA-1 and (c) PBA.

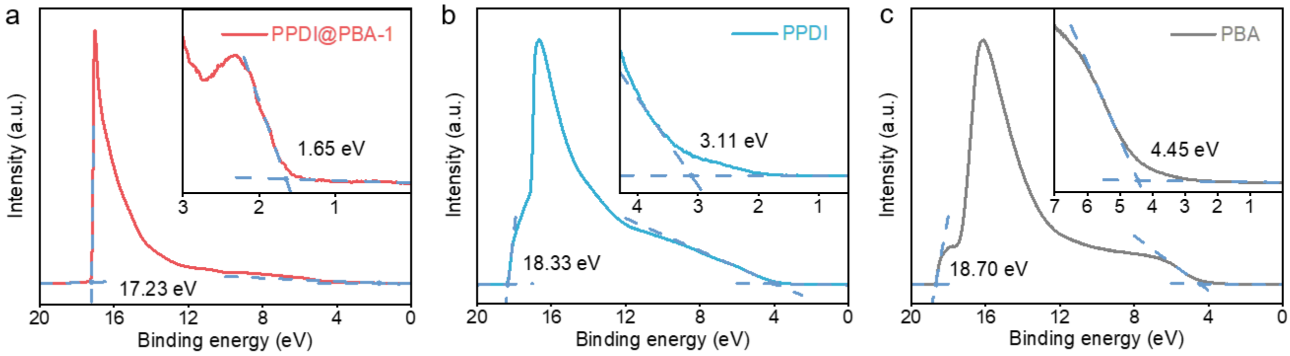

Fig. S14 UPS profiles of (a) PPDI@PBA-1, (b) PPDI and (c) PBA.

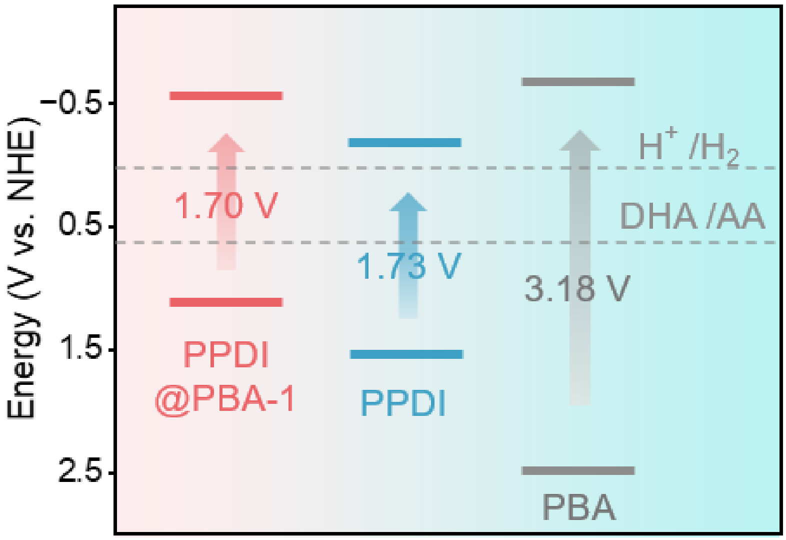

Fig. S15 Energy-level alignments of PPDI@PBA-1, PPDI and PBA.

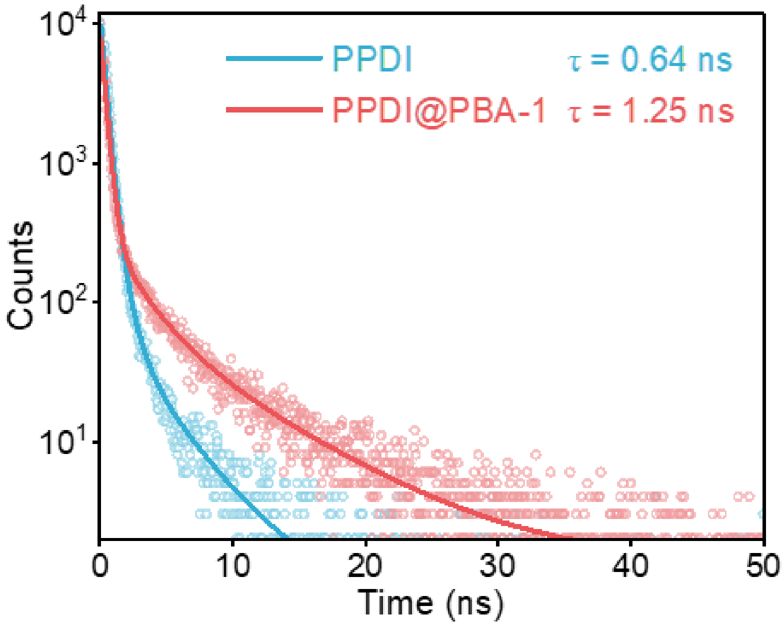

Fig. S16 Time-resolved PL spectra of PPDI and PPDI@PBA-1.

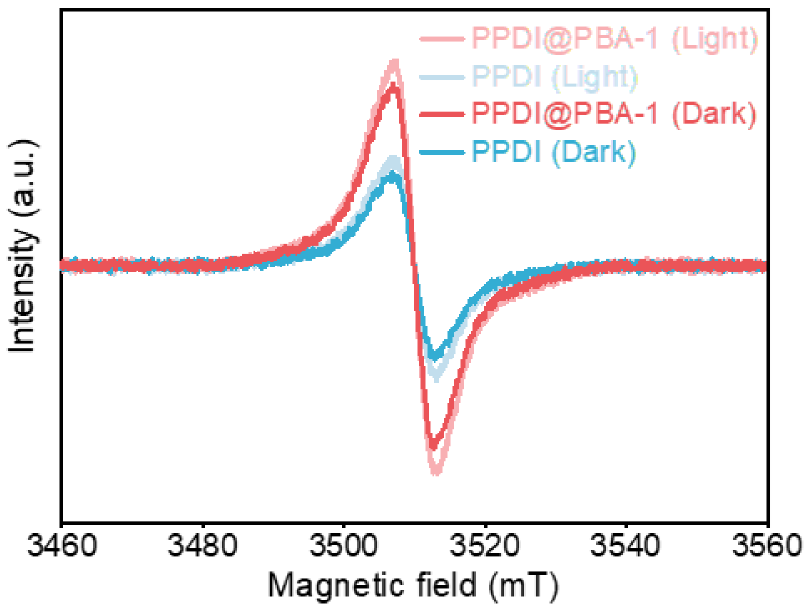

Fig. S17 EPR signals of PPDI and PPDI@PBA-1 under both dark and visible-light irradiation (λ > 420 nm).

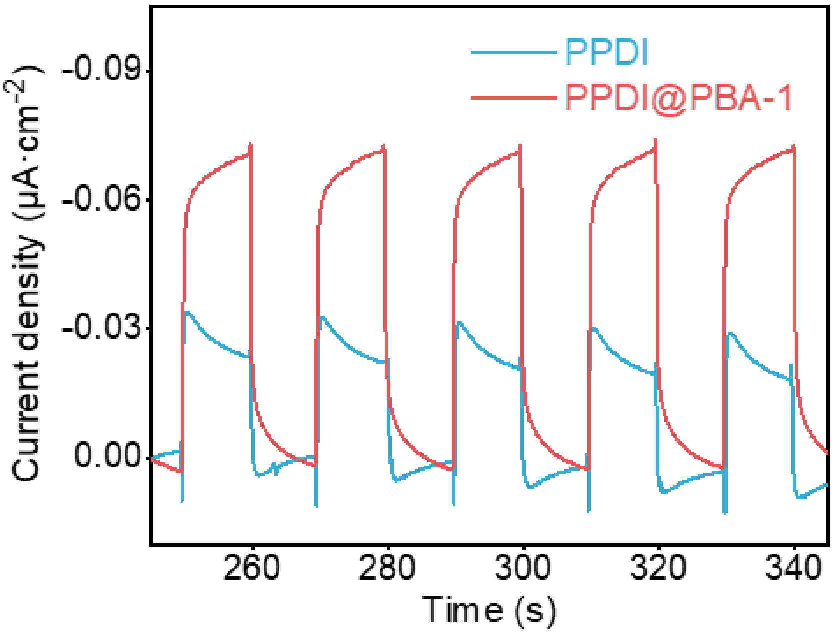

Fig. S18 Photocurrent response of PPDI and PPDI@PBA-1.

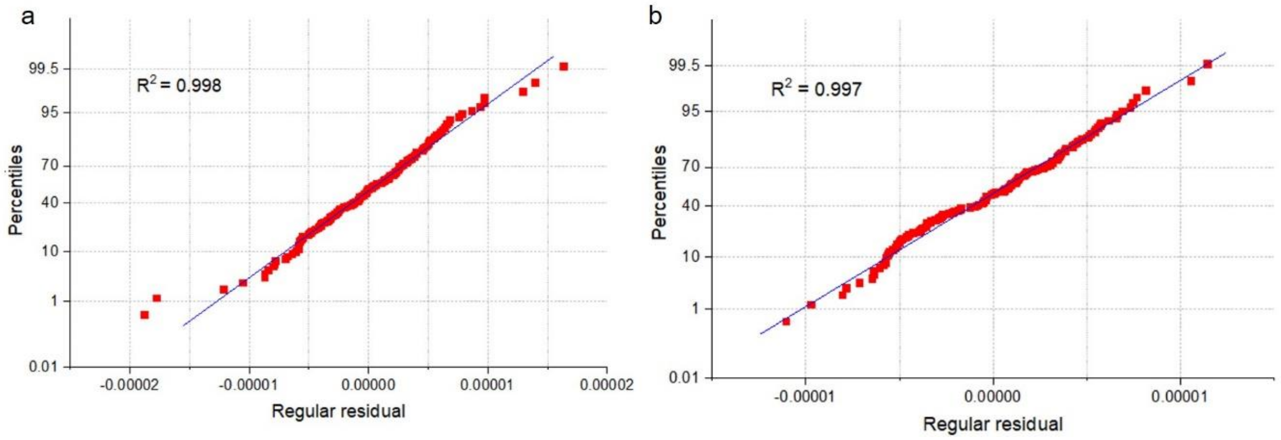

Fig. S19 Rationalization of fitting TAS dynamics using second-order exponential functions.

Note: The average lifetime (τ_{avg}) was calculated from triple exponential function using the following expression:

$$\tau_{avg} = (A_1\tau_1^2 + A_2\tau_2^2) / (A_1\tau_1 + A_2\tau_2)$$

where A_1 and A_2 represent the fitting amplitudes of each decay components, and τ_1 and τ_2 are the values of the corresponding lifetime components. Notably, all the R^2 can reach above 0.99, and the residual analysis shows that the mathematical model has a high confidence level.

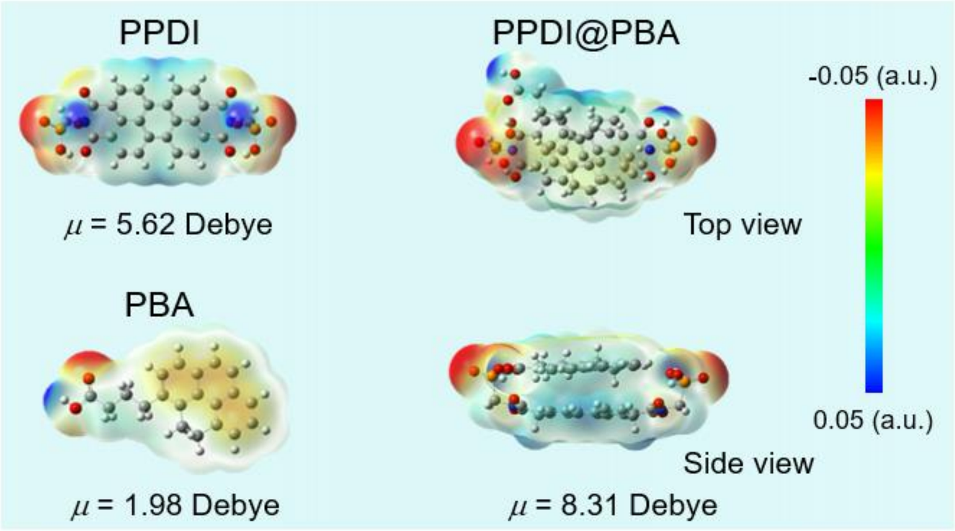

Fig. S20 ESP maps of PPDI, PBA and PPDI@PBA-1.

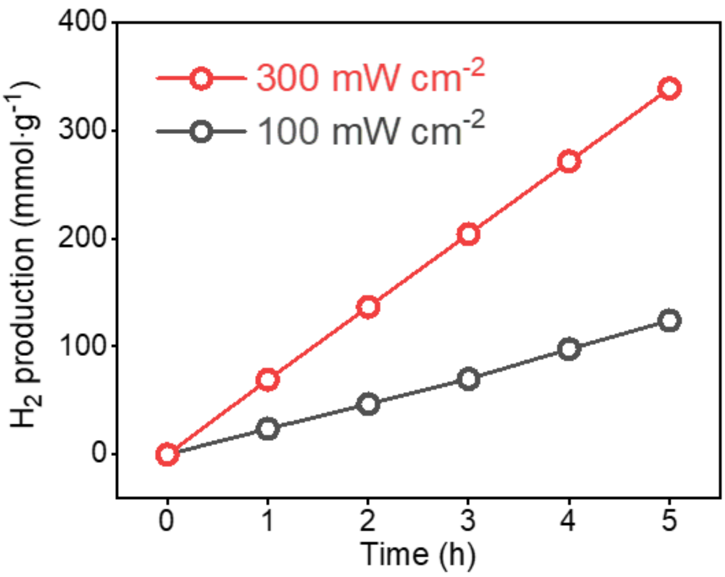

Fig. 21 Time-dependent H_2 production of PPDI@PBA-1 under different illumination intensities (300 and 100 mW cm^{-2}).

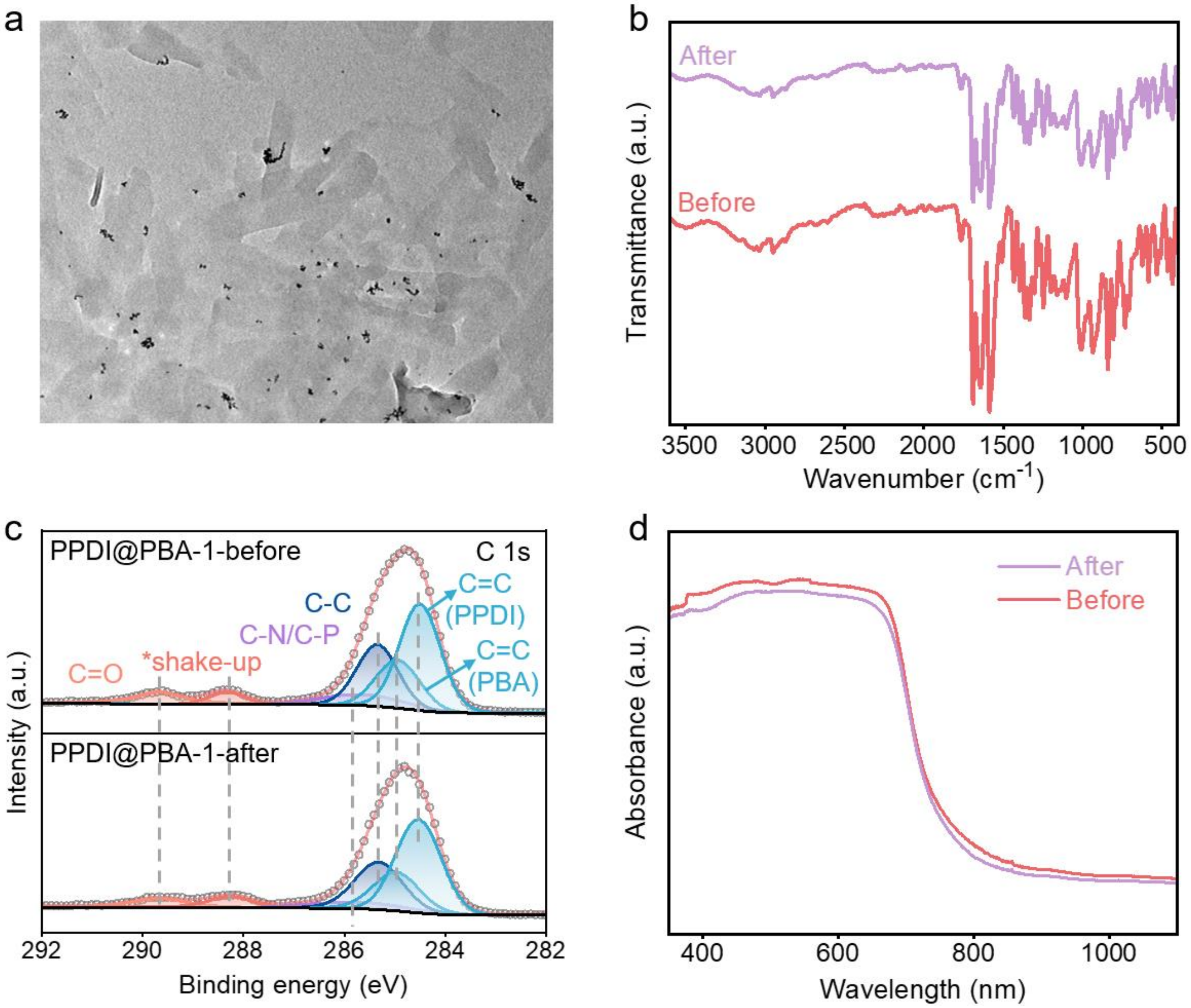

Fig. S22 (a) TEM image of PPDI@PBA-1 recovered after 5 reaction cycles. (b) FT-IR, (c) XPS and (d) UV-vis spectra of PPDI@PBA-1 before and after the cycling tests.

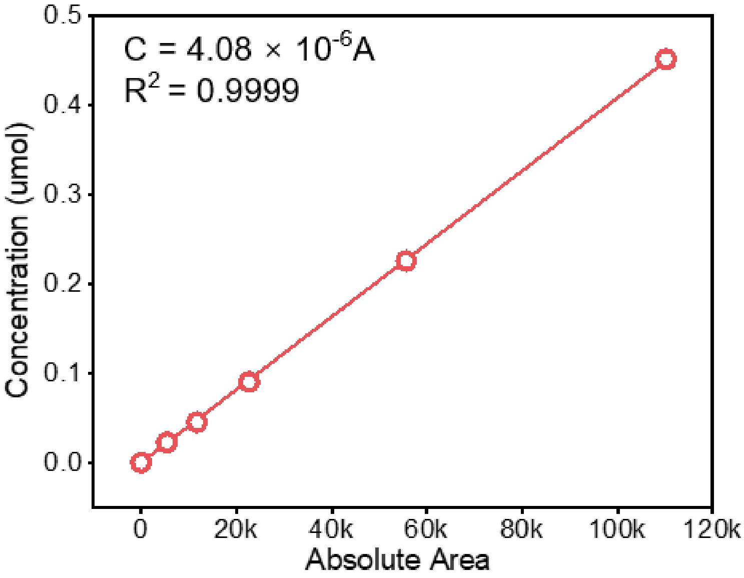

Fig S23 Calibration curve for H_2 quantification.

Supplementary Tables

Table S1 The decay of carrier migration in PPDI and PPDI@PBA-1 monitored at 733 nm.

Sample	**τ_1 (ps)**	**τ_2 (ps)**
PPDI	0.77	20.4
PPDI@PBA-1	77.2	375.6

Table S2 Performance comparison of various organic photocatalysts with D-A architectures.

Catalyst	Co-catalyst	SA	HER (mmol g^{-1} h^{-1})	AQE (%)	Light intensity (mW cm^{-2})	Ref.
PPDI@PBA-1	**Pt**	**AA**	**71.9**	**15.6 (500 nm)**	**300**	**This work**
PPDI@PBA-1	**Pt**	**AA**	**24.8**	**15.6 (500 nm)**	**100**	**This work**
EBE	Pt	TEOA	0.275	2 (400 nm)	-	*Adv. Funct. Mater.* **2023**, *33*, 15
U-t-Bu	Pt	TEOA	0.3699	1.46 (420 nm)	300	*ACS Catal.* **2025**, *15*, 4
NINI-NRs	Pt	TEOA	0.417	1.3 (400 nm)	300	*Angew. Chem. Int. Ed.* 2022, *61*, 12
NDINH/PDINH	Pt	$AgNO_3$	0.3172	3.36 (380 nm)	783	*Angew. Chem. Int. Ed.* **2024**, *63*, 5
P-TP	Pt	TEOA	7.71	8.9 (365 nm)	100	*J. Mater. Chem. A* **2023**, *11*, 5937
TAPPy-DBTDP-COF	Pt	AA	12.7	5 (450 nm)	300	*Adv. Energy Mater.* **2024**, *14*, 40
P-PMPDI	Pt	AA	11.7	2.96 (550 nm)	300	*Chem. Commun.* **2019**, *55*, 8090
LCP-BT	Pt	AA	22	7.8 (420 nm)	300	*Adv. Funct. Mater.* **2024**, *34*, 30
TpaTfa-AC	Pt	AA	20.7	1.43 (450 nm)	300	*Angew. Chem. Int. Ed.* **2021**, *60*, 36
Pt/PMI	Pt	AA	21.2	1.87 (500 nm)	300	*Small* **2025**, *21*, 14
TPPS/PDI	Pt	AA	30.36	3.81 (650 nm)	550	*Adv. Sci.* **2022**, *9*, 17
PTCDA/PTA	Pt	AA	45.06	3.49 (400 nm)	300	*Adv. Funct. Mater.* **2024**, *34*, 17
Py-m-2N	-	TEOA	48.86	0.8 (420 nm)	300	*ACS Nano* **2023**, *17*, 20

BUCT-COF-20	Pt	AA	40.36	2.58 (450 nm)	300	*Angew. Chem. Int. Ed.* **2024**, *63*, 25
P-PMPDI-Zr	Pt	AA	50.46	11.7 (630 nm)	100	*J. Mater. Chem. A* **2021**, *9*, 7675
TCDA-COF	Pt	AA	70.8	3.21 (500 nm)	300	*J. Am. Chem. Soc.* **2023**, *145*, 15

SA, HER, AQE and TEOA refer to sacrificial agent, H_2 evolution rate, apparent quantum efficiency and triethanolamine, respectively.